

Enhancing room-temperature thermoelectricity of $SrTiO_3$ based superlattices via epitaxial strain

Yi Zhu(朱怡), Hao Liu(刘昊), Huilin Lai(赖辉琳), Zhenghua An(安正华), Yinyan Zhu(朱银燕), Lifeng Yin(殷立峰), and Jian Shen(沈健)

Citatio: Chin. Phys. B, 2025, 34 (**9**): 097305. DOI: 10.1088/1674-1056/ade24e
http://cpb.iphy.ac.cn; http://iopscience.iop.org/cpb

What follows is a list of articles you may be interested in

Valley-dependent transport in strain engineering graphene heterojunctions

Fei Wan(万飞), X R Wang(王新茹), L H Liao(廖烈鸿), J Y Zhang(张嘉颜),M N Chen(陈梦南), G H Zhou(周光辉), Z B Siu(萧卓彬), Mansoor B. A. Jalil, and Yuan Li(李源)

Chin. Phys. B, 2022, 31 (**7**): 077302. DOI: 10.1088/1674-1056/ac5613

Topology and ferroelectricity in group-V monolayers

Mutee Ur Rehman, Chenqiang Hua(华陈强), Yunhao Lu(陆赟豪)

Chin. Phys. B, 2020, 29 (**5**): 057304. DOI: 10.1088/1674-1056/ab81ff

Electronic structure of molecular beam epitaxy grown 1T'-$MoTe_2$ film and strain effect

Xue Zhou(周雪), Zeyu Jiang(姜泽禹), Kenan Zhang(张柯楠), Wei Yao(姚维), Mingzhe Yan(颜明哲), Hongyun Zhang(张红云), Wenhui Duan(段文晖), Shuyun Zhou(周树云)

Chin. Phys. B, 2019, 28 (**10**): 107307. DOI: 10.1088/1674-1056/ab43ba

Strain-induced insulator-metal transition in ferroelectric $BaTiO_3$ (001) surface: First-principles study

Lin Yang(杨林), Chang-An Wang(王长安), Cong Liu(刘聪), Ming-Hui Qin(秦明辉), Xu-Bing Lu(陆旭兵), Xing-Sen Gao(高兴森), Min Zeng(曾敏), Jun-Ming Liu(刘俊明)

Chin. Phys. B, 2016, 25 (**7**): 077302. DOI: 10.1088/1674-1056/25/7/077302

Modulation of physical properties of oxide thin films by multiple fields

Hua-Li Yang(杨华礼), Bao-Min Wang(王保敏), Xiao-Jian Zhu(朱小健), Jie Shang(尚杰), Bin Chen(陈斌), Run-Wei Li(李润伟)

Chin. Phys. B, 2016, 25 (**6**): 067303. DOI: 10.1088/1674-1056/25/6/067303

RAPID COMMUNICATION

Enhancing room-temperature thermoelectricity of $SrTiO_3$ based superlattices via epitaxial strain

Yi Zhu(朱怡)[2,3], Hao Liu(刘昊)[2,3], Huilin Lai(赖辉琳)[2,3], Zhenghua An(安正华)[2,3], Yinyan Zhu(朱银燕)[1,2,4,5,§], Lifeng Yin(殷立峰)[1,2,3,4,‡], and Jian Shen(沈健)[1,2,3,4,5,6,†]

[1] *Shanghai Research Center for Quantum Sciences, Shanghai* 201315, *China*
[2] *State Key Laboratory of Surface Physics and Institute for Nanoelectronic Devices and Quantum Computing, Fudan University, Shanghai* 200433, *China*
[3] *Department of Physics, Fudan University, Shanghai* 200433, *China*
[4] *Zhangjiang Fudan International Innovation Center, Shanghai* 201210, *China*
[5] *Hefei National Laboratory, Hefei* 230088, *China*
[6] *Collaborative Innovation Center of Advanced Microstructures, Nanjing* 210093, *China*

(Received 4 May 2025; revised manuscript received 6 June 2025; accepted manuscript online 9 June 2025)

Epitaxial strain is an effective way to control thermoelectricity of a thin film system. In this work, we investigate strain-dependent thermoelectricity of $[(SrTiO_3)_3/(SrTi_{0.8}Nb_{0.2}O_3)_3]_{10}$ superlattices grown on different substrates, including -0.96% on $(LaAlO_3)_{0.3}(SrAl_{0.5}Ta_{0.5}O_3)_{0.7}(001)$ (LSAT), 0% on $SrTiO_3(001)$ (STO), $+0.99\%$ on $DyScO_3(110)$ (DSO) and $+1.64\%$ on $GdScO_3(110)$ (GSO), respectively. Our results show that the highest room-temperature thermoelectricity is achieved when the STO-based superlattice is grown on the DSO substrate with $+0.99\%$ tensile strain. This is attributed to the high permittivity and low dielectric loss arising from the ferroelectric domain and electron–phonon coupling, which boost the power factor (*PF*) to 10.5 $mW{\cdot}m^{-1}{\cdot}K^{-2}$ at 300 K.

Keywords: strain engineering, thermoelectric superlattices, ferroelectricity

PACS: 73.50.Lw, 77.80.–e

DOI: 10.1088/1674-1056/ade24e **CSTR:** 32038.14.CPB.ade24e

1. Introduction

Thermoelectrics, which can directly convert waste heat into electricity through the Seebeck effect, are attracting significant attention as a potential energy harvesting technology.[1–4] The efficiency of thermoelectric materials is determined by a dimensionless figure of merit, $ZT = S^2\sigma T/\kappa$, where T is the absolute temperature, S is the Seebeck coefficient, σ is the electrical conductivity, and κ is the sum of electronic (κ_e) and lattice thermal conductivities (κ_l) of the material. The power factor (*PF*) is equal to $S^2\sigma$, which is used to estimate the performance of thermoelectric power generation. Electronically, since S, σ and κ_e are strongly coupled with each other, improving a single parameter often leads to compensations of the other two, making it difficult to enhance the thermoelectric performance.[4–6]

Fabricating low-dimensional structures is an effective strategy to achieve an enhanced Seebeck coefficient without explicitly reducing σ. Hicks and Dresselhaus[7] predicted the enhancement of S^2 in quantum-well structures due to the increase of density of states near the conduction band edge when the quantum-well thickness becomes less than a few nanometers. Moreover, n-doped $SrTiO_3$ is a promising candidate for thermoelectric devices, as its conduction carriers are more strongly localized than those of the heavy-metal materials.[8] Consequently, great efforts have been made to improve the Seebeck coefficient through the use of low-dimensional structures in $SrTiO_3$-based superlattices.[8–12] Ohta *et al.*[10] clarified that an enhanced two-dimensionality improved thermoelectric power factor to 5 $mW{\cdot}m^{-1}{\cdot}K^{-2}$ at 300 K for $SrTiO_3/SrTi_{0.8}Nb_{0.2}O_3$ superlattices. However, electron diffusion cannot be removed thoroughly in the Nb-doped superlattice structures, resulting in an increased minimum thickness of the barrier layers and a further reduction in the electrical conductivity of the superlattices.

On the other hand, strain-induced band engineering approaches have been proven to be successful for decoupling these parameters for an enhancement in power factor, where the transport bands can be engineered to converge in energy, leading to an increase in electrical conductivity.[13,14] To date, great efforts have been made to improve thermoelectric performance through lattice strain engineering,[15–17] which optimizes the thermoelectric properties of oxides with t_{2g}-active bands.[18] Furthermore, bulk STO is a well-known incipient ferroelectric material, whose ferroelectric phase transi-

†Corresponding author. E-mail: shenj5494@fudan.edu.cn
‡Corresponding author. E-mail: lifengyin@fudan.edu.cn
§Corresponding author. E-mail: zhuyinyan@fudan.edu.cn

© 2025 Chinese Physical Society and IOP Publishing Ltd. All rights, including for text and data mining, AI training, and similar technologies, are reserved.

tion does not occur even at 0 K, due to the competition between quantum fluctuations and ferroelectric order.[19–21] In contrast, a ferroelectric transition of epitaxial films of STO can be induced and modified by the in-plane strain effect.[22–24] Bauer *et al*. predicted a polarization Seebeck and Peltier effect in electrically insulating ordered ferroelectrics that depends strongly on the direction of the ferroelectric order.[25,26] However, few efforts have been made to experimentally explore the effectiveness between the ferroelectric states and thermoelectric performance.

In this work, we combine the strain engineering and the quantum-well effect by fabricating epitaxial $[(STO)_3/(Nb\text{-}STO)_3]_{10}$ superlattices on various substrates to investigate the strain-dependent power factor of STO-based superlattices at room temperature. The room-temperature $|S|$ of the superlattice on DSO is measured to be 292 $\mu V\cdot K^{-1}$, which is greatly larger than that of the superlattices grown on other substrates. Moreover, the STO/DSO superlattice exhibits a high dielectric constant, an elevated ferroelectric transition temperature and a loss tangent of 0.003, which is an order of magnitude smaller than that of the other superlattices. This results in an enhanced density of states yielding the highest PF value of 10.5 $mW\cdot m^{-1}\cdot K^{-2}$. Our work demonstrates how to enhance the thermoelectric performance of epitaxial films using strain-induced ferroelectric transitions, paving the way for designing highperformance oxide-based thermoelectric materials.

2. Experiments

The 25 nm $[(STO)_3/(Nb\text{-}STO)_3]_{10}$ superlattices and STO(001) films were epitaxially grown on LSAT(001), TiO_2-terminated STO(001), DSO(110) and GSO(110) substrates using laser molecular beam epitaxy (ultraviolet laser at 248 nm, 1.5 J/cm^2 fluence, 2 Hz) at 750 °C.[27] The oxygen pressure was kept at 8×10^{-4} mbar during growth. Before growth, all the substrates were acid-etched and thermal-annealed to obtain surfaces with atomically flat terrace structures.[28,29] The growth front of the superlattices and the quality are monitored by *in-situ* reflection high energy electron diffraction (RHEED). Crystallographic analyses of the superlattices were performed by XRD (Cu $K\alpha1$, D8 Discover, Bruker) and AFM (NX10, Paker system). Synchrotron XRD measurements were carried out at beamline BL14B1 of Shanghai Synchrotron Radiation Facility at room temperature, using 18 keV x-rays (0.6887 Å).

Electrical conductivity (σ) was measured at room temperature by a conventional d.c. four-probe method with a van der Pauw geometry in the physical property measurement system (PPMS, Quantum Design). Seebeck coefficient (S) was measured by the thermoelectric parameter test system (MRS-3, JouleYacht). The Seebeck potential (ΔV) and temperature difference (ΔT) were measured simultaneously, and the S values were obtained from the slope of the ΔV–ΔT plots (the correlation coefficient was 0.998). For dielectric permittivity (ε_r) measurements, 100 nm thick Au interdigitated electrodes (IDEs) with 150-μm finger lengths and 8-μm finger gaps were deposited on the 25 nm STO(001) films on various substrates by magneton sputtering. The fingers were aligned parallel to the [100] in-plane directions of the STO films. Measurements of the complex dielectric permittivity were performed on the STO films as a function of temperature T (10–400 K) and direct current electric field E (between +40 V and −40 V across 8 μm) at a measurement frequency (f) of 2 MHz using a LCR meter (E4980A, Keysight). All the ε_r values were obtained after performing similar measurements for all the substrates with equivalent IDEs using a partial capacitance model.[30–33] The model is based on conformally mapping the repeating air–film–substrate units in the IDE geometry to the parallel-plate geometry, as previously reported.[30]

3. Results and discussion

Bulk STO has a cubic $Pm\bar{3}m$ structure with the lattice constant of 3.905 Å (Fig. 1(b)). Depending on the choice of substrate, STO(001) films may be grown under compressive or tensile strain. LSAT is cubic with the lattice constant of $a_{LSAT} = 3.868$ Å, providing an in-plane biaxial compressive strain on STO, as shown in Fig. 1(a). The DSO and the GSO crystals have orthorhombic distorted perovskite structures with the space group $Pbnm$. The DSO(110) and the GSO(110) substrates can be considered as a pseudo-cubic structure with in-plane lattice constants of $a_{DSO} = 3.944$ Å and $a_{GSO} = 3.970$ Å, respectively, providing in-plane biaxial tensile strain on the STO, as shown in Fig. 1(c). The epitaxial relationship is $[001]_{PC}$ STO$\|[110]_O$ DSO and $[010]_{PC}$ STO$\|[001]_O$ DSO. Hence, as shown in Fig. 1, the corresponding in-plane strain $\varepsilon = (a_{sub} - a_{STO})/a_{sub}$ for the STO(001) films is −0.96% on LSAT, 0% on STO, +0.99% on DSO and +1.64% on GSO.

Figure 2(a) shows AFM morphological images of the 25 nm superlattices grown on all substrates. Clear atomic steps are observed in the AFM images, with each atomic terrace having a height of approximately 0.4 nm, and no cracks or film discontinuities are observed. The reciprocal space map (RSM) images show good alignment between the in-plane lattices of the superlattices and different substrates (Fig. 2(b)). To determine the lattice constants of the superlattices grown on different substrates, XRD analysis was conducted. In Fig. 2(c), high-resolution x-ray diffraction measurements reveal that the (002) peaks of the superlattices shift to higher angles when the strain changes from compressive to tensile. As a result, the out-of-plane lattice constants of the $[(STO)_3/(Nb\text{-}STO)_3]_{10}$ superlattices at room temperature are $a_\perp = 3.931$ Å on LSAT, 3.909 Å on STO, 3.899 Å on DSO, and 3.880 Å on GSO. Both the superlattice satellite peaks and the thickness fringes indicate the high degree of interface abruptness in the samples.

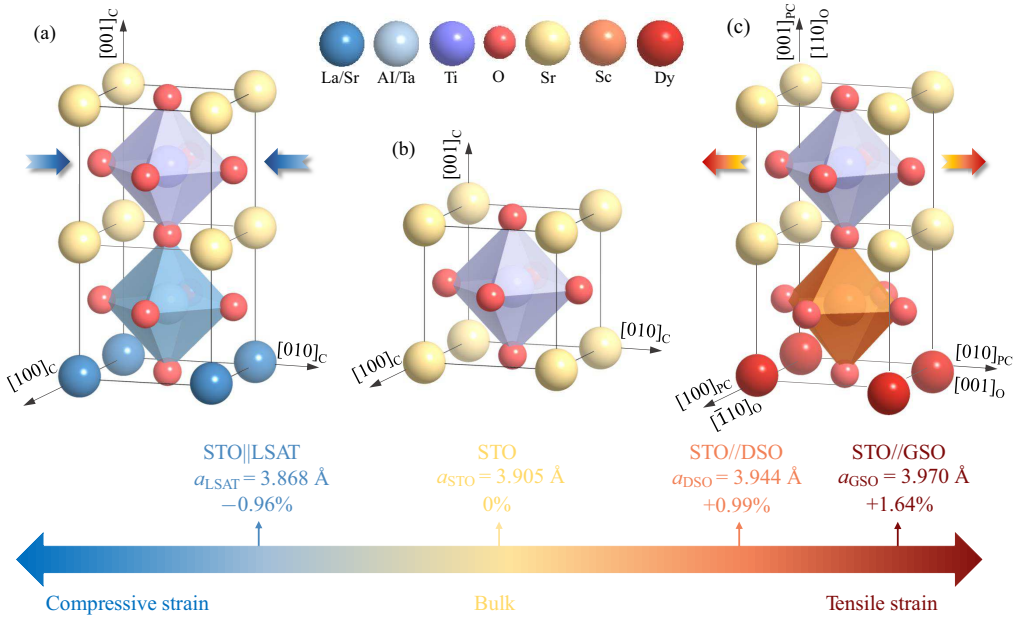


Fig. 1. Strained STO(001) films on different substrates. (a) The strained STO(001) film on the cubic unit cell LSAT(001) substrate. (b) The cubic unit cell of STO bulk. (c) The strained STO(001) film on the pseudo cubic DSO(110) substrate. The ScO_6 octahedron is tilted for illustration.

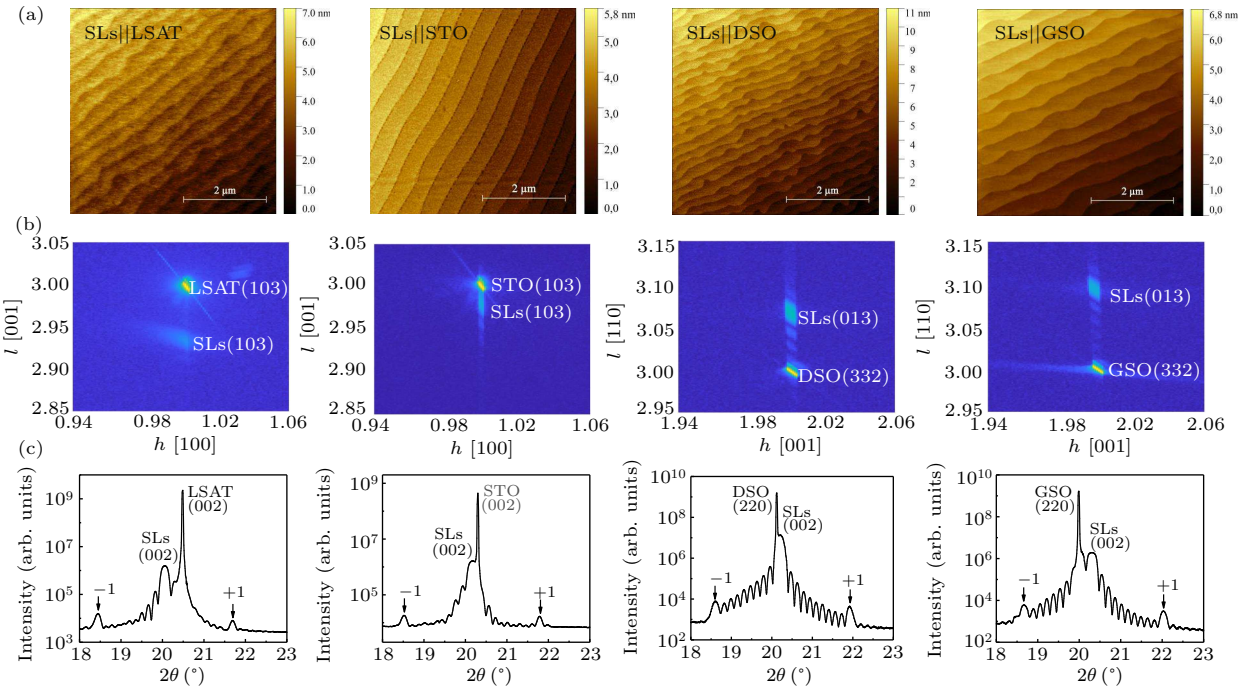


Fig. 2. Morphology and structure analysis of the $[(STO)_3/(Nb\text{-}STO)_3]_{10}$ superlattices on different substrates. (a) Atomic terraces of average step height $\bar{d} \sim 0.4$ nm are observed via 5 μm×5 μm AFM images of the superlattices on different substrates. (b) High-resolution reciprocal space maps (RSMs) of the superlattices around the asymmetric Bragg reflections on LSAT(103), STO(103), DSO(332) and GSO(332). (c) High resolution short angular-range θ–2θ XRD scan of the superlattice centered on the (002) superlattices peak. The labels and arrows mark the superlattice satellite peaks.

The thermoelectric properties of the superlattices were determined based on the measurements of electrical conductivity (σ) and Seebeck coefficient (S). Figure 3(a) summarizes the electrical conductivity as a function of temperature (σ–T) for the superlattices under different strains, ranging from −0.96% (LSAT) to +1.64% (GSO). The highest conductivity of the superlattice reached 4.9×10^5 S·m^{-1} at room temperature for the unstrained superlattice in Fig. 3(d). Metallic behavior is suppressed in the strained superlattices, which are characterized by much lower σ and insulating behavior at low temperatures, depending sensitively on the magnitude and sign of the strain. For small strain, the conductivity of the superlattices tends to be larger under tensile strain than that under compressive strain due to the enhanced carrier mobility and lower effective mass near the bottom of the conduction band (E_{CB}).[34–38] This enhancement may be caused by the tensile strain-induced breaking of the t_{2g} orbital degeneracy, leading to suppression of the phonon–electron scattering rates and in-

crease of mobility.[34–37] For tensile strain, the lowest band maintains mainly light-electron character and exhibits lower effective mass than that of compressive strain for transport along the in-plane directions.[38] For large strain, the superlattice under larger strain (GSO +1.64%) exhibits more insulating behavior than that under smaller strain (DSO +0.99%). These results suggest that epitaxial strain plays a key role in driving the insulating behavior.

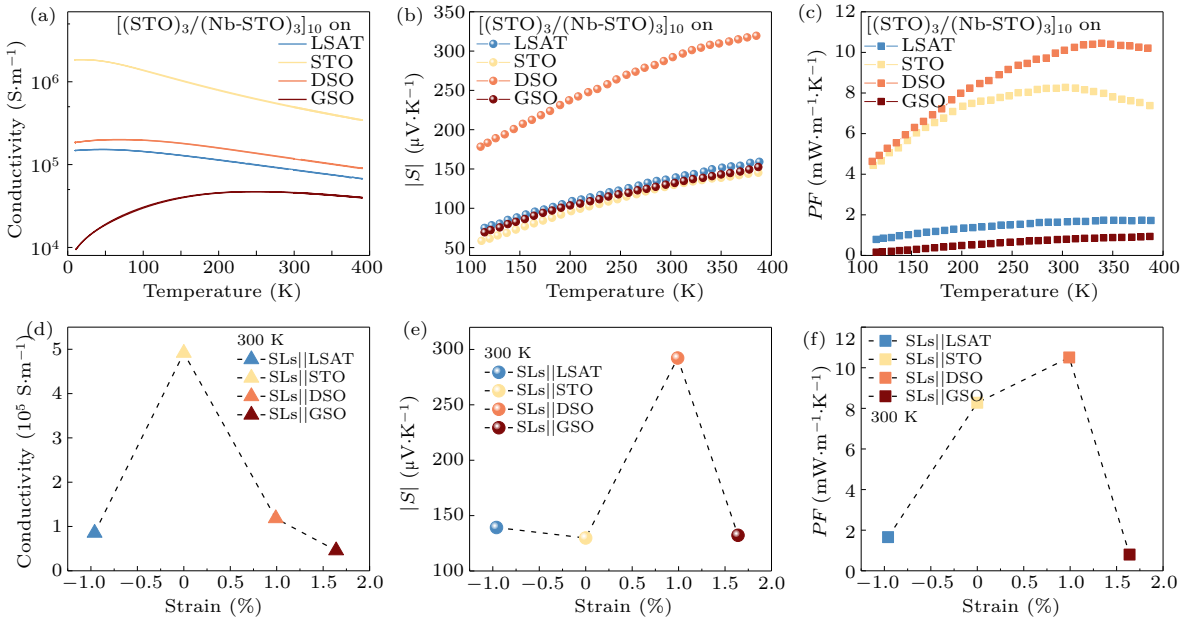


Fig. 3. Electrical and thermoelectrical properties of the $[(STO)_3/(Nb\text{-}STO)_3]_{10}$ superlattices on different substrates. Temperature dependence of (a) electrical conductivity, (b) absolute Seebeck coefficient, and (c) power factor. Room-temperature (d) electrical conductivity, (e) absolute Seebeck coefficient, (f) power factor of the $[(STO)_3/(Nb\text{-}STO)_3]_{10}$ superlattice under different strains.

The Seebeck coefficient is negative over the entire temperature range for all superlattices, indicating that the majority charge carriers are electrons. Figure 3(b) shows the temperature-dependent $|S|$ of the STO-based superlattices with four different strains. In general, the $|S|$ value increases monotonically with the temperature due to the fact that the chemical potential decreases.[39] At elevated temperatures, the slope becomes smaller and finally saturates, indicating that there is a narrow conduction band near E_F.[40] Noticeably, the $|S|$ value for the superlattice on DSO (tensile strain +0.99%) is 292 $\mu V \cdot K^{-1}$ at room temperature in Fig. 3(e), which is significantly larger than that of the other strained superlattices in the entire temperature range. Such large enhancement of $|S|$ suggests that a strong electron confinement can be achieved at small tensile strain by utilizing the highly directional Ti 3d (t_{2g}) orbitals, where the direct overlap between neighboring 3d orbitals is relatively small, and carrier electrons tend to localize on the Ti atom.[8,41] For the unstrained superlattice on STO, the $|S|$ is determined to be 130 $\mu V \cdot K^{-1}$ at 300 K, which is relatively close to that of the bulk Nb-STO ($|S| = 108$ $\mu V \cdot K^{-1}$), indicating that the confinement effect is greatly suppressed because of higher electrical conductivity and higher carrier concentration.[42] In stark contrast, strain has little positive effect on the Seebeck coefficients of the superlattices grown on LSAT and GSO, suggesting that the inhibited electron behavior of the superlattices on these two substrates cannot be solely attributed to the carrier concentration. Instead, the electron density of states (DOS) near the bottom of the conduction band and the two-dimensional electronic confinement should be considered.

The calculated partial DOS of Nb 4d or Ti 3d in the STO/Nb-STO superlattice indicates that the electron carriers can seep from the Nb-STO layers into the $SrTiO_3$ layers.[10,42] Such electron diffusion to the neighboring STO layers, especially in the d_{xz} and d_{yz} bands, reduces the two-dimensionality and weakens the electron confinement in the quantum wells.[43] Therefore, the capability for binding electrons of the barrier STO layers becomes more important in the thermopower behaviors. Moreover, the abundant ferroelectric states coupled with strong dielectric responses could be effectively manipulated through the substrate engineering in STO films.[23]

In order to further demonstrate the relationship of the thermoelectric properties with the strain states and ferroelectric transition, we study the dielectric properties of the STO(001) films on LSAT, DSO and GSO substrates and compare them with bulk STO. Bulk STO is an incipient ferroelectric,[19–21] and with decreasing temperature, the dielectric constant and loss tangent simultaneously increase as shown in Figs. 4(a) and 4(b). No obvious dielectric response of electric field is observed in Fig. 4(d). For compressive strain, the STO film on the LSAT substrate suppresses the in-plane ferroelectric transition, resulting in a decreased dielectric constant, an increased loss tangent, and no observable peak in

the temperature-dependent dielectric response. The reduced dielectric constant disrupts the potential barrier walls of the quantum well, leading to electron leakage and a low Seebeck coefficient. Additionally, the dielectric constant shows no response to the electric field in Fig. 4(c), suggesting that the TO1 mode becomes harder and further electron–phonon coupling is suppressed.[37]

For tensile strain, the STO film on the DSO substrate possesses the highest dielectric constant of 9000 at T_C, the lowest dielectric loss tangent of 0.003 and 88% dielectric tuning at 50 kV·cm^{-1} (Figs. 4(a), 4(b) and 4(d)), indicating its extraordinary capability of electron confinement. The smooth peak at $T_C = 264$ K in Fig. 4(a) evidences a soft polar phonon mode driven ferroelectric transition and strong electron–phonon coupling.[24,44–46] Moreover, bipolar cycles at different measurement temperatures reveal that $\varepsilon_r(E)$ (Fig. 4(e)) displays a peak near T_C and splits below T_C due to ferroelectric hysteresis. The inset shows the magnified $\varepsilon_r(E)$ at 260 K, where the splitting behavior can still be seen. In case of large tensile strain, the STO film on the GSO substrate possesses a significantly increased loss tangent (~ 0.02) and reduced dielectric tuning ($\sim 15\%$ with a 50 kV·cm^{-1}) at room temperature, with a higher T_C above 400 K and a broader width of the peak. Additionally, the split bipolar cycles persist until 400 K, but dielectric tuning is suppressed with temperature possibly due to the onset of antiferrodistortive phase transition and the rotated directions of ferroelectric polarization.[47] The high dielectric losses are likely one of the reasons for the leakage current and decreased $|S|$ of the commensurately strained superlattice on GSO, which weaken the quantum well effect. Moreover, the large tensile strain of the GSO splits the threefold orbital degeneracy to a singlet degenerate state and distorts the TiO_6 octahedron. This structural rearrangement is likely to weaken the Ti–O bands, narrow the total density of states and consequently degrade the thermopower.[48,49]

Therefore, combining the results of the Seebeck coefficient and electrical conductivity, we calculated the temperature-dependent *PF* values as shown in Fig. 3(c). The *PF* values of the $[(STO)_3/(Nb\text{-}STO)_3]_{10}$ superlattice on DSO are significantly improved across all temperature ranges due to the larger Seebeck coefficient, reaching 10.5 mW·m^{-1}·K^{-2} at 300 K as shown in Fig. 3(f), which doubles the value of the STO-based superlattice in previous work.[10] According to the significant reduction in the thermal conductivity induced by the ferroelectric transition and phonon softening, the *ZT* values of the $[(STO)_3/(Nb\text{-}STO)_3]_{10}$ superlattice reached 1.2 at room temperature, as reported in our previous work.[12]

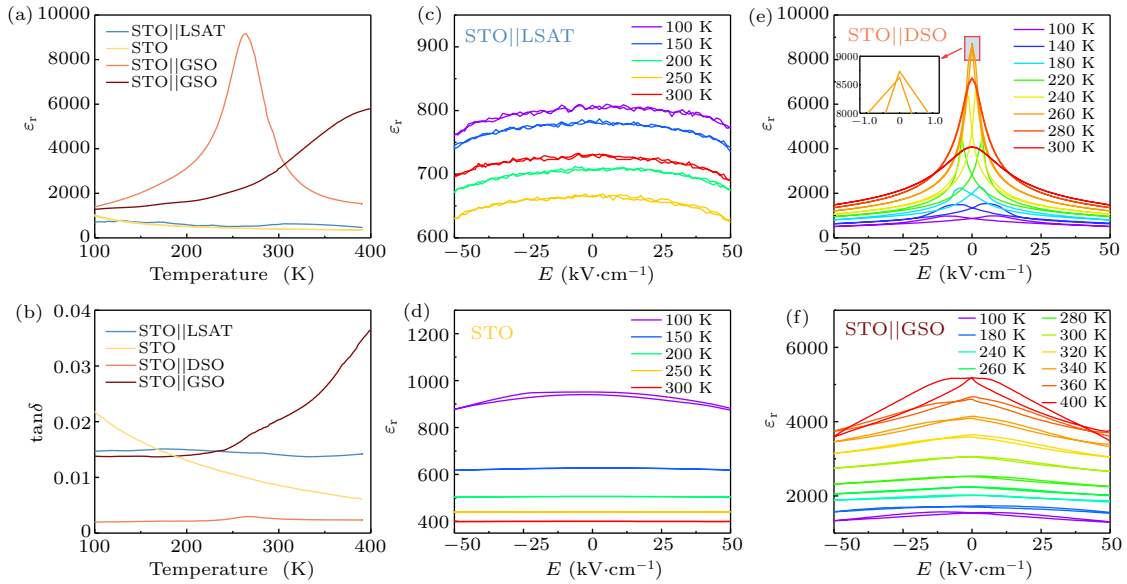


Fig. 4. In-plane dielectric response of the strained STO film. (a) Temperature-dependent dielectric constant for bulk STO and STO(001) films fabricated on LSAT, DSO and GSO. (b) Temperature-dependent dielectric loss tangent for bulk STO and STO(001) films fabricated on LSAT, DSO and GSO. (c)–(f) Dielectric response of electrical field obtained at 2 MHz while sweeping the bias field at $f \approx 1$ Hz for bulk STO and STO(001) films fabricated on LSAT, DSO and GSO, respectively.

4. Conclusions

Epitaxial oxide films offer large areas of high-quality crystalline material in a single orientation, yet they are rarely used to study thermoelectric effects. In this work, we demonstrate that introducing small tensile strain into the STO-based superlattices increases the ferroelectric transition temperature, leading to an enhanced quantum well effect and improved electron–phonon coupling at elevated temperatures, which in turn enhances their room-temperature thermoelectric properties. A large *PF* value of 10.5 mW·m^{-1}·K^{-2} has been achieved at room temperature for the $[(STO)_3/(Nb\text{-}STO)_3]_{10}$ superlattice under 0.99% tensile strain. Excitingly, T_C of the ferroelectric phase transition can also be increased by applying tensile strain to a laminated freestanding STO membrane

after being transferred to a stretchable polymer substrate,[50] which provides great potentials in high-performance wearable thermoelectric devices. We conclude that combining the strain engineering approach with the phonon-glass electron-crystal strategy is effective to design excellent oxide-based thermoelectric materials with high thermoelectric power factor, opening new possibilities for advancing many other thermoelectrics.

Acknowledgements

We thank beamline BL14B1 (Shanghai Synchrotron Radiation Facility) for providing the beam time and help during experiments. This work is supported by the National Key Research & Development Program of China (Grant No. 2022YFA1403300), the Innovation Program for Quantum Science and Technology (Grant No. 2024ZD0300103), the National Natural Science Foundation of China (Grant Nos. 11991060, 11427902, 12074075, 62171136, and 12474165), the Shanghai Municipal Science and Technology Major Project (Grant No. 2019SHZDZX01), and the Shanghai Municipal Natural Science Foundation (Grant Nos. 22ZR1407400, 22ZR1408100, and 23ZR1407200).

References

[1] DiSalvo F J 1999 *Science* **285** 703
[2] Vining C B 2009 *Nat. Mater.* **8** 83
[3] Zhang Q, Deng K, Wilkens L, Reith H and Nielsch K 2022 *Nature Electronics* **5** 333
[4] Snyder G J and Toberer E S 2008 *Nat. Mater.* **7** 105
[5] Zhu T, Liu Y, Fu C, Heremans J P, Snyder J G and Zhao X 2017 *Adv. Mater.* **29** 1605884
[6] Yang L, Chen Z G, Dargusch M S and Zou J 2018 *Advanced Energy Materials* **8** 1701797
[7] Hicks L D and Dresselhaus M S 1993 *Phys. Rev. B* **47** 12727
[8] Ohta H, Kim S, Mune Y, Mizoguchi T, Nomura K, Ohta S, Nomura T, Nakanishi Y, Ikuhara Y, Hirano M, Hosono H and Koumoto K 2007 *Nat. Mater.* **6** 129
[9] Abutaha A I, Kumar S R S, Li K, Dehkordi A M, Tritt T M and Alshareef H N 2015 *Chem. Mater.* **27** 2165
[10] Zhang Y Q, Feng B, Hayashi H, Chang C P, Sheu Y M, Tanaka I, Ikuhara Y and Ohta H 2018 *Nat. Commun.* **9** 2224
[11] Mune Y, Ohta H, Koumoto K, Mizoguchi T and Ikuhara Y 2007 *Appl. Phys. Lett.* **91** 192105
[12] Zhu Y, Wang W, Liang B, Liu W, Zhou T, Meng B, Liu H, Gao W, Yang Y, Niu C, Zheng C, An Z, Wu S, Liu W, Zhang Y, Yuan C, Zhu Y, Yin L and Shen J 2025 *J. Mat. Chem. C* **13** 2279
[13] Liu W, Tan X, Yin K, Liu H, Tang X, Shi J, Zhang Q and Uher C 2012 *Phys. Rev. Lett.* **108** 166601
[14] Pei Y, Shi X, LaLonde A, Wang H, Chen L and Snyder G J 2011 *Nature* **473** 66
[15] Wu Y, Chen Z, Nan P, Xiong F, Lin S, Zhang X, Chen Y, Chen L, Ge B and Pei Y 2019 *Joule* **3** 1276
[16] Lou X, Li S, Chen X, Zhang Q, Deng H, Zhang J, Li D, Zhang X, Zhang Y, Zeng H and Tang G 2021 *ACS Nano* **15** 8204
[17] Guo S D 2016 *J. Mat. Chem. C* **4** 9366
[18] Fumega A O and Pardo V 2017 *J. Phys.: Condens. Matter* **29** 065501
[19] Müller K A and Burkard H 1979 *Phys. Rev. B* **19** 3593
[20] Neville R C, Hoeneisen B and Mead C A 1972 *J. Appl. Phys.* **43** 2124
[21] Servoin J L, Luspin Y and Gervais F 1980 *Phys. Rev. B* **22** 5501
[22] Haeni J H, Irvin P, Chang W, Uecker R, Reiche P, Li Y L, Choudhury S, Tian W, Hawley M E, Craigo B, Tagantsev A K, Pan X Q, Streiffer S K, Chen L Q, Kirchoefer S W, Levy J and Schlom D G 2004 *Nature* **430** 758
[23] Pertsev N A, Tagantsev A K and Setter N 2000 *Phys. Rev. B* **61** R825
[24] Li Y L, Choudhury S, Haeni J H, Biegalski M D, Vasudevarao A, Sharan A, Ma H Z, Levy J, Gopalan V, Trolier-McKinstry S, Schlom D G, Jia Q X and Chen L Q 2006 *Phys. Rev. B* **73** 184112
[25] Bauer G E W, Iguchi R and Uchida K I 2021 *Phys. Rev. Lett.* **126** 187603
[26] Tang P, Iguchi R, Uchida K I and Bauer G E W 2022 *Phys. Rev. Lett.* **128** 047601
[27] Ye B, Miao T, Zhu Y, Huang H, Yang Y, Shuai M, Zhu Z, Guo H, Wang W, Zhu Y, Yin L and Shen J 2021 *Rev. Sci. Instrum.* **92** 113906
[28] Kawasaki M, Takahashi K, Maeda T, Tsuchiya R, Shinohara M, Ishiyama O, Yonezawa T, Yoshimoto M and Koinuma H 1994 *Science* **266** 1540
[29] Kleibeuker J, Kuiper B, Harkema S, Koster G, Rijnders G, Tinnemans P, Vlieg E, Rossen P, Portale G, Ravichandran J and Ramesh R 2012 *Phys. Rev. B* **85** 165413
[30] Zhang S, Deliyore-Ramírez J, Deng S, Nair B, Pesquera D, Jing Q, Vickers M E, Crossley S, Ghidini M, Guzmán-Verri G G, Moya X and Mathur N D 2024 *Nat. Mater.* **23** 639
[31] Vendik O G, Zubko S P and Nikol'ski M A 1999 *Technical Physics* **44** 349
[32] Biegalski M D 2006 *Epitaxialy Strained Strontium Titanate* (PhD thesis) (The Pennsylvania State Univ.)
[33] Gevorgian S S, Martinsson T, Linner P L J and Kollberg E L 1996 *IEEE Trans. Microwave Theory Tech.* **44** 896
[34] Zou D F, Liu Y Y, Xie S H, Lin J G and Li J Y 2013 *Chem. Phys. Lett.* **586** 159
[35] Jalan B, Allen S J, Beltz G E, Moetakef P and Stemmer S 2011 *Appl. Phys. Lett.* **98** 132102
[36] Verma A, Kajdos A P , Cain T A , Stemmer S and Jena D 2014 *Phys. Rev. Lett.* **112** 216601
[37] Himmetoglu B, Janotti A, Peelaers H, Alkauskas A and Van de Walle C G 2014 *Phys. Rev. B* **90** 241204
[38] Janotti A, Steiauf D and Van de Walle C G 2011 *Phys. Rev. B* **84** 201304
[39] Ohta S, Nomura T, Ohta H and Koumoto K 2005 *J. Appl. Phys.* **97** 034106
[40] Amin B, Singh N, Tritt T M, Alshareef H N and Schwingenschlögl U 2013 *Appl. Phys. Lett.* **103** 031907
[41] Hung N T, Hasdeo E H, Nugraha A R T, Dresselhaus M S and Saito R 2016 *Phys. Rev. Lett.* **117** 036602
[42] Zhang Y, Feng B, Hayashi H, Tohei T, Tanaka I, Ikuhara Y and Ohta H 2017 *J. Appl. Phys.* **121** 185102
[43] Blöchl P E 1994 *Phys. Rev. B* **50** 17953
[44] Lee J H, Fang L, Vlahos E, *et al.* 2010 *Nature* **466** 954
[45] Nuzhnyy D, Petzelt J, Kamba S, Kužel P, Kadlec C, Bovtun V, Kempa M, Schubert J, Brooks C M and Schlom D 2009 *Appl. Phys. Lett.* **95** 232902
[46] Biegalski M D, Vlahos E, Sheng G, Li Y L, Bernhagen M, Reiche P, Uecker R, Streiffer S K, Chen L Q, Gopalan V, Schlom D G and Trolier-McKinstry S 2009 *Phys. Rev. B* **79** 224117
[47] Vasudevarao A, Denev S, Biegalski M D, Li Y, Chen L Q, Trolier-McKinstry S, Schlom D G and Gopalan V 2008 *Appl. Phys. Lett.* **92** 192902
[48] Fumega A O and Pardo V 2017 *J. Phys.: Condens. Matter* **29** 065501
[49] Huang Z, Liu Z Q, Yang M, Zeng S W, Annadi A, Lü W M, Tan X L, Chen P F, Sun L, Renshaw Wang X, Zhao Y L, Li C J, Zhou J, Han K, Wu W B, Feng Y P, Coey J M D, Venkatesan T and Ariando 2014 *Phys. Rev. B* **90** 125156
[50] Xu R J, Huang J W, Barnard E S, Hong S S, Singh P, Wong E K, Jansen T, Harbola V, Xiao J, Wang B Y, Crossley S, Lu D, Liu S and Hwang H Y 2020 *Nat. Commun.* **11** 3141